Estimation of The Microstructure & Properties of Ferritic Creep–Resistant Steels

H. K. D. H. Bhadeshia

University of Cambridge
Department of Materials Science and Metallurgy
Pembroke Street, Cambridge CB2 3QZ, U.K.

Abstract

Creep resistant steels must be reliable over very long periods of time in severe environments. Their microstructures have to be very stable, both in the wrought and in the welded states. This paper reviews the quantitative methods for the design of steels for elevated temperature applications. A methodology is described for the calculation of complex precipitation reactions over periods extending many tens of years. However, microstructure alone is not enough in the design of alloys. The estimation of the creep rupture stress using a neural network technique is described in the second part of this review. The calculation of the influence of solute–elements on the self–diffusivity of iron, which features in many creep equations, is an emerging area in alloy design. The methodology for such calculations is reviewed in the final section of the paper.

Introduction

Typical operating parameters for steels used in the manufacture of power plant are compared against corresponding values for nickel alloys in aeroengines, in Table 1. In both cases, the service conditions are severe. But this is especially so for steels where the service life is many decades. The degree of reliability demanded of heat resistant steels is therefore extraordinary, and must represent one of the highest achievements of technology. By contrast, computers, which are frequently identified with advanced technology, seldom last for more than two years and are generally obsolete at the point of installation!

Property	Aeroengine	Power Plant
Temperature	$> 1000\,°C$	540-750 °C
Pressure	$\simeq 3$ bar	160–370 bar
Design life	10^4 h	2.5×10^5 h
$\sigma_{100,000\ h}$	10 MPa	100 MPa
Coating	Yes	No
Forced cooling	Yes	No
Single crystal	Yes	No

Table 1: Service conditions for a component in the hot part of an aeroengine and one in the hottest part of a power plant. The lower limits for the power plant component are representative of current technology. The stress is a 100,000 h creep rupture strength.

It should not be surprising that the number of variables involved in the design of creep–resistant steels is very large – in fact, we shall show later that there are at least thirty parameters which need to be controlled in any experiment or calculation of creep properties.

The variables can ideally be taken into account using what scientists like to call "physical models", *i.e.* theories which explain a large class of observations, which contain few arbitrary elements and which make verifiable predictions. The first part of this paper deals with such physical models in the prediction of microstructure.

There is no adequate theory to deal with the second task, which is the estimation of creep rupture strength as a function of the steel composition, microstructure and heat treatment. Difficult problems like this, where the general concepts might be understood but which are not as yet amenable to fundamental treatment, are common in metallurgy. To form a complete design–technology, it is consequently necessary to resort to careful empiricism. The second part of this paper deals with a semi–empirical method implemented to achieve useful results. The combination of physical and empirical models can then be used to attempt the design of alloys.

The final part of the paper deals with the estimation of the self–diffusion coefficient of iron containing solute additions. This is perceived to be an important parameter in creep deformation; it has become prominent in recent work because of the availability of commercial software capable of estimating the diffusivity. It is useful therefore to summarise the basis of such calculations, even though it is too early to comment on their significance in the context of changes in creep properties.

The Microstructure

There is a large variety of heat–resistant steels (Table 2). The ones with the lowest solute concentrations might contain substantial quantities of allotriomorphic ferrite and some pearlite, but the vast majority have bainitic or martensitic microstructures in the normalised condition. After normalising the steels are severely tempered to produce a "stable" microstructure consisting of a variety of alloy carbides in a ferritic matrix. The known precipitates are listed in Fig. 1; they determine the microstructure and are crucial in the development of creep strain. The task is therefore to model the evolution of precipitation and dissolution reactions.

The results of equilibrium calculations which give the phase fractions of the carbides as a function of the overall alloy composition and temperature, are given in Fig. 2 for the common power plant steels. The calculations have been done using the *MTDATA* [1] computer program and *SGTE* database, taking into account the carbide phases and Laves phase listed, together with cementite. The chemical elements considered are carbon, silicon, manganese, chromium, nickel, molybdenum, vanadium, niobium and nitrogen. M_5C_2 has recently been identified in 1Cr–0.5Mo steels [2] but along with graphite, has not been included in the analysis.

Equilibrium calculations such as those presented in Fig. 2 are useful in specifying the ultimate microstructure but the results are far from the actual microstructures that exist during service. It is necessary in practice to be able to calculate time–temperature–transformation diagrams for tempering reactions, as a function of steel chemical composition and tempering temperature. In order to do this, a theory capable of handling several simultaneous precipitation reactions has been developed [4], where the different phases influence each other, for example by drawing the same solute from the matrix ferrite.

Overall transformation kinetics

A model for a single transformation begins with the calculation of the nucleation and growth rates using classical theory, but an estimation of the volume fraction requires impingement

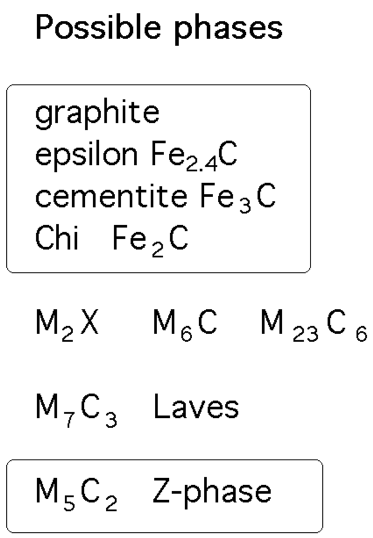

Fig. 1: The variety of precipitates to be found in power plant steels. The iron–rich carbides such as cementite form extremely rapidly, whereas graphite forms incredibly slowly because it is difficult to nucleate. M_5C_2 and Z–phase are recent discoveries [2,3].

between particles to be taken into account. This is generally done using the extended volume concept of Johnson, Mehl, Avrami, and Kolmogorov [5] as illustrated in Fig. 3. Suppose that two particles exist at time t; a small interval δt later, new regions marked a, b, c & d are formed assuming that they are able to grow unrestricted in extended space whether or not the region into which they grow is already transformed. However, only those components of a, b, c & d which lie in previously untransformed matrix can contribute to a change in the real volume of the product phase (identified by the subscript '1') so that :

$$dV_1 = (1 - \frac{V_1}{V})dV_1^e \tag{1}$$

where it is assumed that the microstructure develops randomly. The superscript e refers to extended volume, V_1 is the volume of phase 1 and V is the total volume. Multiplying the change in extended volume by the probability of finding untransformed regions has the effect of excluding regions such as b, which clearly cannot contribute to the real change in volume of the product. This equation can easily be integrated to obtain the real volume fraction,

$$\frac{V_1}{V} = 1 - \exp\left\{-\frac{V_1^e}{V}\right\} \tag{2}$$

Nucleation and growth rates can readily be substituted into V_1^e, leading to the familiar Avrami equation.

In practice, there are many cases where several transformations occur together. The different reactions interfere with each other in a way which is seminal to the development of power plant microstructures. The principles involved are first illustrated with an example in which β and θ precipitate at the same time from the parent phase which is designated α. For the sake of discussion it is assumed that the nucleation and growth rates do not change with time and that the particles grow isotropically.

Designation	C	Si	Mn	Ni	Mo	Cr	V
1Cr$\frac{1}{2}$Mo	0.15	0.25	0.50	–	0.6	0.95	
$\frac{1}{4}$CrMoV	0.15	0.25	0.50	0.05	0.50	0.30	0.25
$\frac{1}{2}$Cr$\frac{1}{2}$Mo$\frac{1}{4}$V	0.12	0.25	0.50	–	0.6	0.45	0.25
1CrMoV	0.25	0.25	0.75	0.70	1.00	1.10	0.35
2$\frac{1}{4}$Cr1Mo	0.15	0.25	0.50	0.10	1.00	2.30	0.00
Mod. 2$\frac{1}{4}$Cr1Mo	0.1	0.05	0.5	0.16	1.00	2.30	0.25
						Ti=0.03	B=0.0024
3.0Cr1.5Mo	0.1	0.2	1.0	0.1	1.5	3.0	0.1
3.5NiCrMoV	0.24	0.01	0.20	3.50	0.45	1.70	0.10
9Cr1Mo	0.10	0.60	0.40	–	1.00	9.00	–
Mod. 9Cr1Mo	0.1	0.35	0.40	0.05	0.95	8.75	0.22
					Nb=0.08	N=0.05	Al <0.04
9Cr$\frac{1}{2}$MoWV	0.11	0.04	0.45	0.05	0.50	9.00	0.20
					W=1.84	Nb=0.07	N=0.05
12CrMoV	0.20	0.25	0.50	0.50	1.00	11.25	0.30
12CrMoVW	0.20	0.25	0.50	0.50	1.00	11.25	0.30
							W=0.35
12CrMoVNb	0.15	0.20	0.80	0.75	0.55	11.50	0.28
						Nb 0.30	N 0.06

Table 2: Typical compositions (wt.%) of creep–resistant steels. The range of alloys available is in fact much larger than this, for example, there is a variety of alloys available for bolting applications.

The increase in the extended volume due to particles nucleated in a time interval $t = \tau$ to $t = \tau + d\tau$ is, therefore, given by

$$dV^e_\beta = \frac{4}{3}\pi G^3_\beta (t-\tau)^3 I_\beta(V)\ d\tau \tag{3}$$

$$dV^e_\theta = \frac{4}{3}\pi G^3_\theta (t-\tau)^3 I_\theta(V)\ d\tau \tag{4}$$

where G_β, G_θ, I_β and I_θ are the growth and nucleation rates of β and θ respectively, all of which are assumed here to be independent of time. V is the total volume of the system. For each phase, the increase in extended volume will consist of three separate parts. Thus, for β:

(i) β which has formed in untransformed α.

(ii) β which has formed in regions which are already β.

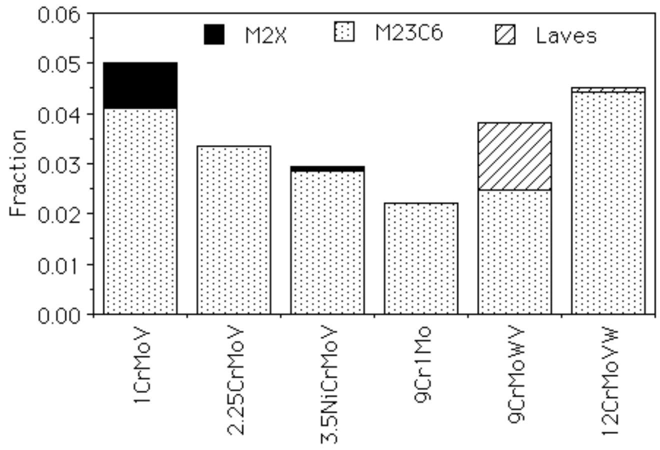

Fig. 2: Equilibrium fractions of carbides in some common power plant steels, as calculated using MTDATA and the SGTE thermodynamic database for 565 °C (838 K). Very small fractions of vanadium and niobium carbonitrides are are present in some steels but are not shown. Thus, the modified 9Cr1Mo contains 0.0009 NbN and 0.003 VN, the 9CrMoWV steel contains 0.0008 NbN and 0.0032 VN. The calculations allowed the existence of all the carbides described in Figure 1 with the exception of graphite, epsilon, Chi, Z–phase and M_5C_2.

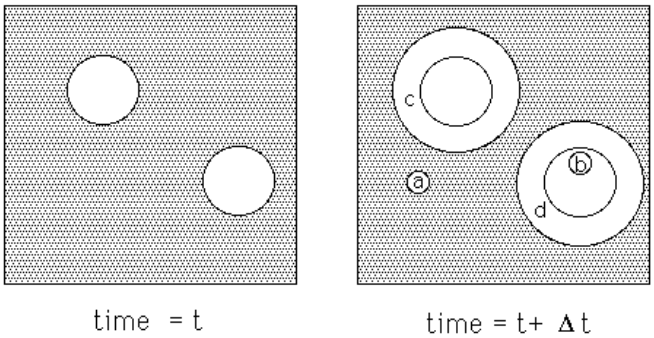

Fig. 3: The concept of extended volume. Two precipitate particles have nucleated and grown to a finite size in the time t. New regions c and d are formed as the original particles grow, but a & b are new particles, of which b has formed in a region which is already transformed.

(iii) β which has formed in regions which are already θ.

Only β formed in untransformed α will contribute to the real volume of β. On average a fraction $\left(1 - \frac{V_\beta + V_\theta}{V}\right)$ of the extended volume will be in previously untransformed material. It follows that the increase in real volume of β is given by

$$dV_\beta = \left(1 - \frac{V_\beta + V_\theta}{V}\right) dV^e_\beta \qquad (5)$$

and similarly for θ,

$$dV_\theta = \left(1 - \frac{V_\beta + V_\theta}{V}\right) dV^e_\theta \qquad (6)$$

V_β is expected to be some complicated function of V_θ so it is not generally possible to integrate these expressions analytically to find the relationship between the real and extended volumes. Numerical integration is straightforward and offers the opportunity to change the boundary conditions for nucleation and growth as transformation proceeds, to account for the change in the matrix composition during the course of reaction. The method can in principle be applied to any number of simultaneous reactions.

Complex reactions The multiple reactions found in power plant steels have important complications which can all be dealt with in the scheme of simultaneous transformations as presented above. The phases interfere with each other not only by reducing the volume available for transformation, but also by removing solute from the matrix and thereby changing its composition. This change in matrix composition affects the growth and nucleation rates of the phases. The main features of the application of the theory to power plant steels are summarised below; a full description is given in references [4].

- The model allows for the simultaneous precipitation of M_2X, $M_{23}C_6$, M_7C_3, M_6C and Laves phase. M_3C is assumed to nucleate instantaneously with the paraequilibrium composition [6]. Subsequent enrichment of M_3C as it approaches its equilibrium composition is accounted for.
- All the phases, except M_3C, form close to their equilibrium composition. The driving forces and compositions of the precipitating phases are calculated using MTDATA [1].
- The interaction between the precipitating phases is accounted for by considering the change in the average solute level in the matrix as each phase forms.
- The model does not require prior knowledge of the precipitation sequence.
- Dissolution of non–equilibrium phases is incorporated as a natural event.
- A single set of fitting parameters for the nucleation equations (site densities and surface energies) has been found which is applicable to a wide range of power plant steels.

The compositions of three power plant alloys used here for illustration purposes, are shown in Table 3. These three alloys, whilst of quite different chemical compositions, show similar precipitation *sequences* [4,7,8] but with vastly different rates. For example, at 600 °C the time taken before $M_{23}C_6$ is observed is 1 h in the 10CrMoV steel [4], 10 h in the 3Cr1.5Mo alloy [7] and in excess of 1000 h in the $2\frac{1}{4}$Cr1Mo steel [8]. These differences have never before been explained prior to the simultaneous transformations model [4].

Microstructure Calculations

A plot showing the predicted variation of volume fraction of each precipitate as a function of time at 600 °C is shown in Fig. 4. Consistent with experiments, the precipitation kinetics

	C	N	Mn	Cr	Mo	Ni	V	Nb
$2\frac{1}{4}$Cr1Mo	0.15	–	0.50	2.12	0.9	0.17	–	–
3Cr1.5Mo	0.1	–	1.0	3.0	1.5	0.1	0.1	–
10CrMoV	0.11	0.056	0.50	10.22	1.42	0.55	0.20	0.50

Table 3: Concentration (in weight%) of the major alloying elements in the steels used to demonstrate the model.

of $M_{23}C_6$ are predicted to be much slower in the $2\frac{1}{4}$Cr1Mo steel compared to the 10CrMoV and 3Cr1.5Mo alloys. One contributing factor is that in the $2\frac{1}{4}$Cr1Mo steel a relatively large volume fraction of M_2X and M_7C_3 form prior to $M_{23}C_6$. These deplete the matrix and therefore suppress $M_{23}C_6$ precipitation. The volume fraction of M_2X which forms in the 10CrMoV steel is relatively small, and there remains a considerable excess of solute in the matrix, allowing $M_{23}C_6$ to precipitate rapidly. Similarly, in the 3Cr1.5Mo steel the volume fractions of M_2X and M_7C_3 are insufficient to suppress $M_{23}C_6$ precipitation to the same extent as in the $2\frac{1}{4}$Cr1Mo steel.

$M_{23}C_6$ is frequently observed in the form of coarse particles which are less effective in hindering creep deformation. Delaying its precipitation would have the effect of stabilising the finer dispersions of M_2X and MX to longer times with a possible enhancement of creep strength.

Calculations like these can be used to design microstructures exploiting knowledge built up over decades concerning what is good and bad for creep strength. It is often argued that Laves phase formation is bad for creep resistance – it leads to a reduction in the concentration of solid solution strengthening elements; since the Laves precipitates are few and coarse, they do not themselves contribute significantly to strength. The model presented here can be used to design against Laves phase formation.

We note for the moment, that this is as far as microstructure modelling has progressed. The models are not yet capable of giving size distributions and even if that were to be possible, there are no physical models of creep deformation which have sufficient precision to make use of this information. We shall not be discouraged by this since good empirical methods are available. The work described below originates from research by Brun *et al.* [9] and Cole and Bhadeshia [10].

Creep Rupture Strength – the Variables

The basic principles of alloy design for creep resistance are well–established and well–founded on experience. The steels must have a stable microstructure which contains fine alloy carbides to resist the motion of dislocations; however, changes are inevitable over the long service time so that there must be sufficient solid solution strengthening to ensure long term creep resistance. There may be other requirements such as weldability, corrosion and oxidation resistance. It is nevertheless difficult to express the design process quantitatively given the large number of interacting variables.

These variables are described later in the context of calculations in Table 4. For the moment we note that the entire information about microstructure and properties is in principle locked up in this set of parameters since chemical composition and heat treatment are comprehensively included. There may, of course, be many other independent variables that might be considered important in creep analysis, but these are for the moment neglected for two reasons. Firstly, an empirical analysis requires experimental data; an over ambitious list would simply reduce the dataset since publications frequently do not report all of the necessary parameters. Secondly,

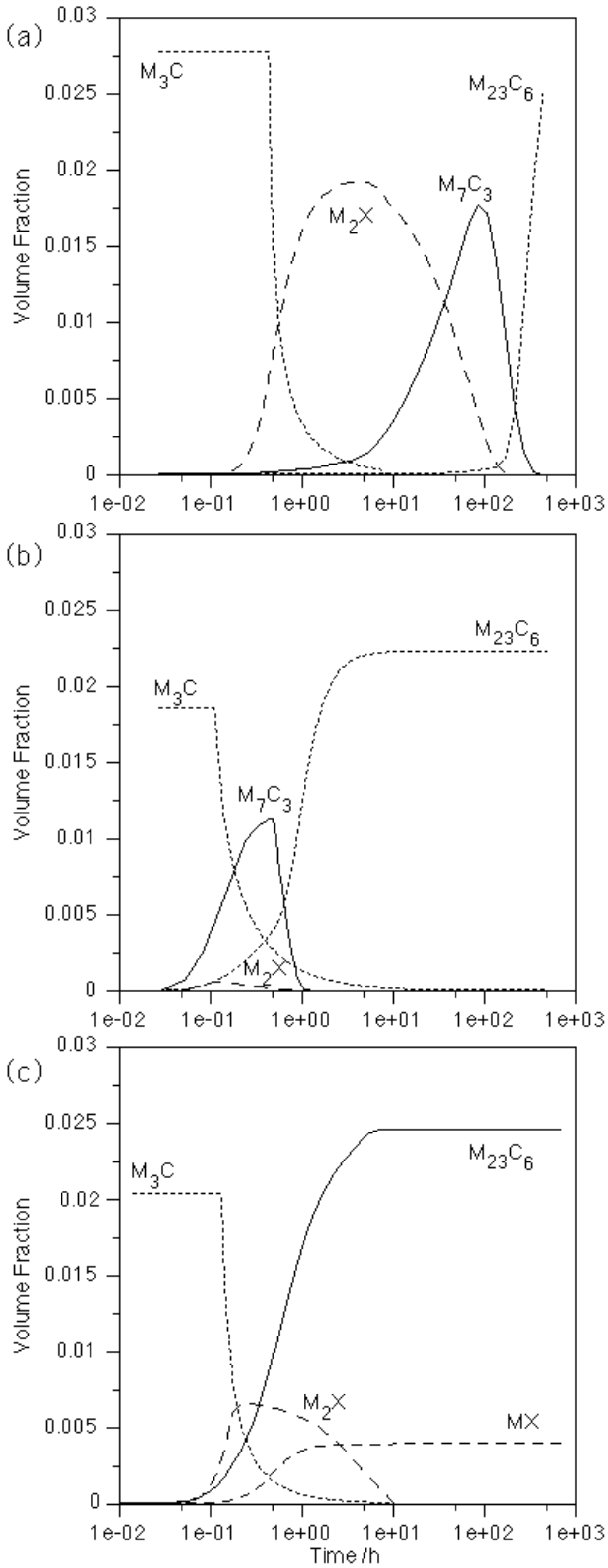

Fig. 4: The predicted evolution of precipitate volume fractions at 600 °C for three power plant materials (a) $2\frac{1}{4}$Cr1Mo (b) 3Cr1.5Mo and (c) 10CrMoV.

the effect of any missing variables would simply be reflected in the uncertainties of prediction. If the predictions are noisy then they can be improved with carefully designed experiments at a future date. Bearing this in mind, the results to be presented are based on some 2000 sets of experiments obtained from the published literature. We now proceed to describe briefly the methodology.

The Neural Network Method

Most people are familiar with regression analysis where data are best–fitted to a specified relationship which is usually linear. The result is an equation in which each of the inputs x_j is multiplied by a weight w_j; the sum of all such products and a constant θ then gives an estimate of the output $y = \sum_j w_j x_j + \theta$. It is well understood that there are dangers in using such relationships beyond the range of fitted data.

A more general method of regression is neural network analysis. As before, the input data x_j are multiplied by weights, but the sum of all these products forms the argument of a hyperbolic tangent. The output y is therefore a non–linear function of x_j, the function usually chosen being the hyperbolic tangent because of its flexibility. The exact shape of the hyperbolic tangent can be varied by altering the weights (Fig. 5a). Further degrees of non–linearity can be introduced by combining several of these hyperbolic tangents (Fig. 5b), so that the neural network method is able to capture almost arbitrarily non–linear relationships. For example, it is well known that the effect of chromium on the microstructure of steels is quite different at large concentrations than in dilute alloys. Ordinary regression analysis cannot cope with such changes in the form of relationships.

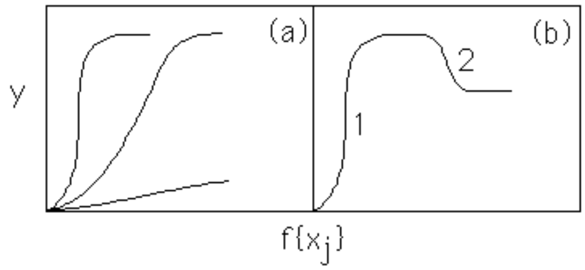

Fig. 5: (a) Three different hyperbolic tangent functions; the "strength" of each depends on the weights. (b) A combination of two hyperbolic tangents to produce a more complex model.

A potential difficulty with the use of powerful regression methods is the possibility of overfitting data (Fig. 6). For example, one can produce a neural network model for a completely random set of data. To avoid this difficulty, the experimental data can be divided into two sets, a *training* dataset and a *test* dataset. The model is produced using only the training data. The test data are then used to check that the model behaves itself when presented with previously unseen data.

Neural network models in many ways mimic human experience and are capable of learning or being trained to recognise the correct science rather than nonsensical trends. Unlike human experience, these models can be transferred readily between generations and steadily developed to make design tools of lasting value. These models also impose a discipline on the digital storage of valuable experimental data, which may otherwise be lost with the passage of time.

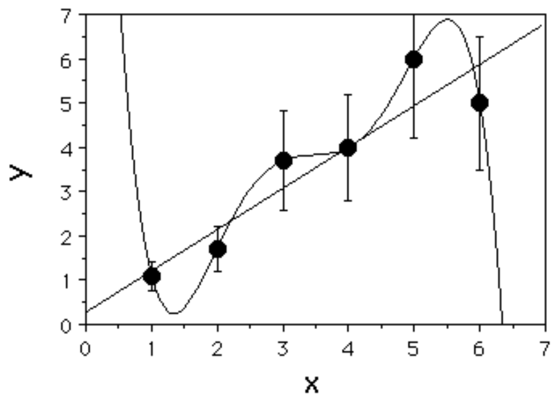

Fig. 6: A complicated model may overfit the data. In this case, a linear relationship is all that is justified by the noise in the data.

The technique is extremely powerful and useful. Its application to creep rupture strength analysis is presented below. The details can be found elsewhere [11] but it is important to note that the generalisation of the model on unseen data has been tested extensively against large quantities of information.

Calculations of Creep Rupture Strength

Fig. 7 shows the variation in the creep rupture strength (10^5 h) of a modern "10CrMoW" creep resistant steel (Table 4) as a function of the temperature, carbon, chromium and molybdenum concentrations. The error bounds represent the uncertainty in fitting the non–linear function to the training data, as 65% confidence limits. There is an additional error associated with each calculation, which is the noise in the experimental data, which is perceived to be of the order of $\pm 2\%$. The engineering design of power plant is based on the ability to support a stress of 100 MPa for 10^5 h at the service temperature. The apparent insensitivity of the creep rupture strength to the molybdenum or chromium concentrations for 10^5 h is not surprising given that the carbides will all be extremely coarse at that stage of life.

Similar data for the classical $2\frac{1}{4}$Cr1Mo steel are illustrated in Fig. 8. The fitting uncertainties are smaller in this case because of the larger quantity of available data since this alloy has been available and studied for a much longer time.

Calculations like these can now be routinely carried out. Furthermore, the models can be improved both as more data become available and as creep deformation becomes better understood. The model can be used in a variety of ways. The combined application of the physical models presented earlier, and the neural network model has led to predictions of novel alloys which ought to have much better creep resistance than any comparable commercial alloy [9]. There are long–term experiments in progress to test these designer–alloys. Another way is to apply the models to welding alloys, for which there are much fewer data when compared with wrought steels.

Welding Alloys

Weld metals and steels of matching composition seem to have similar creep rupture properties. In fact, the chemical compositions of weld metals and corresponding steel plates are not very different (Table 5). Of course, weld metal will have a higher oxygen and nitrogen

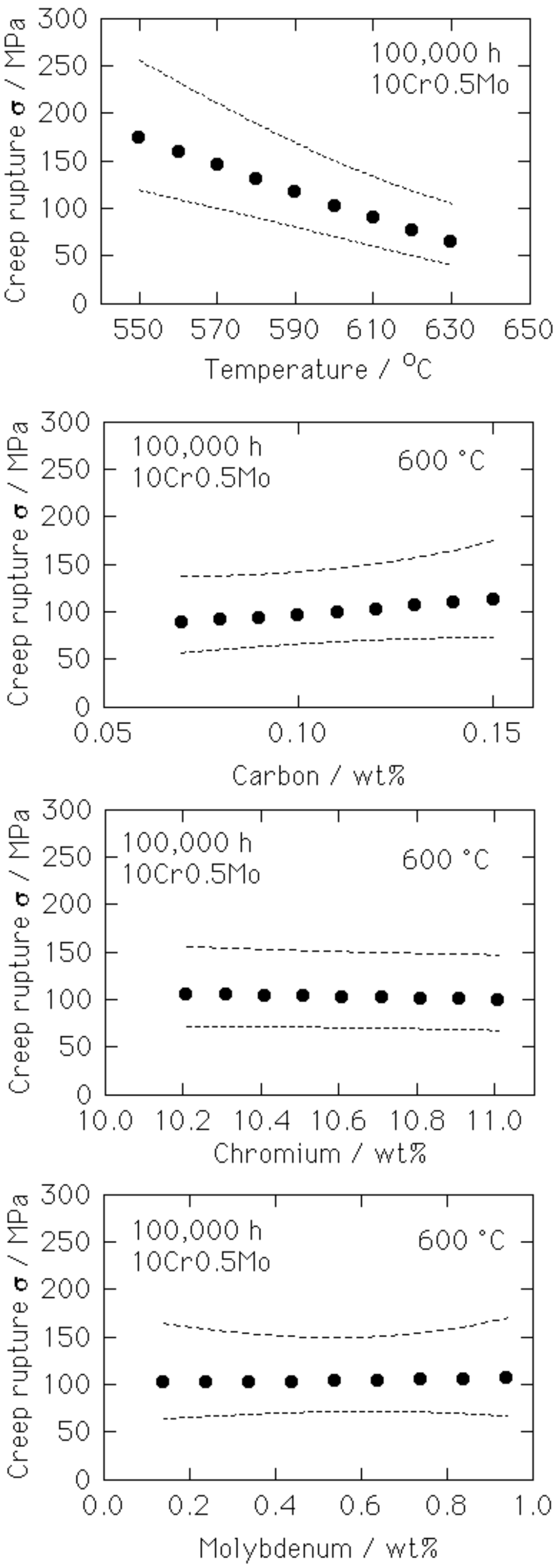

Fig. 7: Creep rupture stress at 600 °C and 100,000 h for 10Cr–0.5Mo type steel

[12].

STEEL	$2\frac{1}{4}$CrMo	10CrMoW
Normalising temperature / K	1203	1338
Duration / h	6	2
Cooling rate	water quenched	air cooled
Tempering temperature / K	908	1043
Duration / h	6	4
Cooling rate	air cooled	air cooled
Annealing temperature / K	873	1013
Duration / h	2	4
Cooling rate	air cooled	air cooled
C wt%	0.15	0.12
Si	0.21	0.05
Mn	0.53	0.64
P	0.012	0.016
S	0.012	0.001
Cr	2.4	10.61
Mo	1.01	0.44
W	0.01	1.87
Ni	0.14	0.32
Cu	0.16	0.86
V	0.01	0.21
Nb	0.005	0.01
N	0.0108	0.064
Al	0.018	0.022
B	0.0003	0.0022
Co	0.05	0.015
Ta	0.0003	0.0003
O	0.01	0.01

Table 4: The standard set of input parameters for two alloys used to examine trends predicted by the neural network. The chemical compositions are all in wt.%

concentration but the former should not affect creep resistance. Although differences in the nitrogen concentration are important, they can easily be taken into account both in predicting carbonitride formation and in the neural network model where nitrogen is an input.

The microstructure of an as–deposited weld metal is naturally radically different from that of a wrought steel. However, even this is unimportant because of the severe tempering heat treatments used following the welding procedure, essentially wipe out the original microstructure and replace it with one which is tempered and similar to that of the steel plate. It is probably for this reason that the welding process itself is found not to influence the creep rupture life [12].

The hypothesis can be proved by examining the data on all–weld metal tests in the published

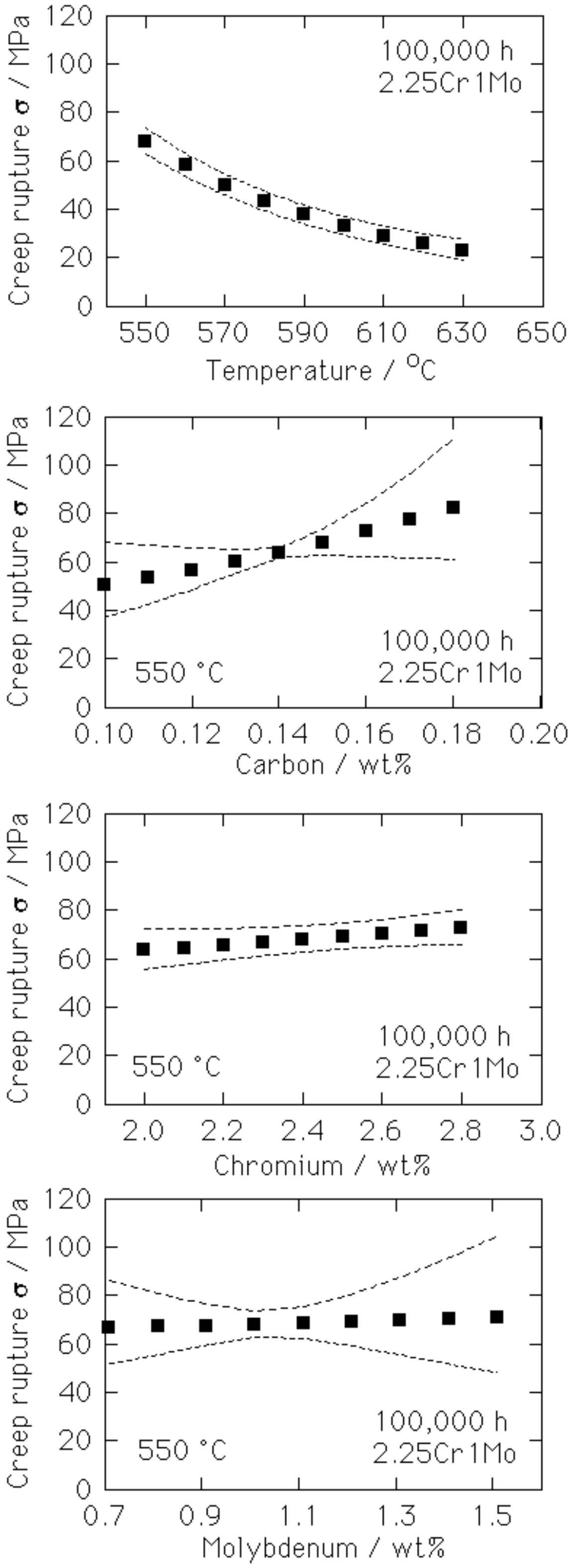

Fig. 8: Creep rupture stress for 2.25Cr–1Mo type steel

	2.25Cr1Mo		9Cr1Mo	
wt.%	Plate	Weld	Plate	Weld
C	0.110	0.091	0.110	0.090
Mn	0.390	0.590	0.040	0.480
Si	0.290	0.300	0.460	0.500
Cu	0.150	0.024		
Ni	0.150	0.033	0.050	0.050
Cr	2.070	2.480	8.960	8.700
Mo	0.900	1.170	0.470	0.980
Nb			0.069	0.040
V	0.004	0.015	0.200	0.200
S	0.022	0.014		
P	0.011	0.010		
N	0.005	0.010	0.051	0.040
O	0.005	0.030	0.005	0.030

Table 5: Chemical compositions, wt%.

literature [12], again for a stress rupture life of 10^5 h. Such data are most reliable for the $2\frac{1}{4}$Cr1Mo type weld metals; the calculations are therefore presented for the $2\frac{1}{4}$Cr1Mo weld metal listed in Table 5.

Fig. 9 shows the very encouraging agreement between the calculated [9,10] and measured [12] creep rupture lives of $2\frac{1}{4}$Cr1Mo welds. The predictions are made without any adjustment of the models, which did not interrogate any weld metal data during their creation. The results confirm that it is reasonable to assume that weld metal creep rupture life can be modelled on the basis of wrought steels. Of course, other properties such as creep ductility may be more sensitive to inclusion content in which case the weld metals should exhibit a lower ductility relative to the wrought steel.

The method can now be used to generate creep–rupture diagrams such as that illustrated in Fig. 10.

Self–Diffusion in Iron

The way in which solutes affect the diffusivity of iron atoms must be of importance in creep theory. The estimation of these effects is now becoming possible although the significance of the calculations in the context of design against creep has yet to be established. We discuss here the methodology for the calculations without commenting on their importance, which is best determined experimentally. As usual, things are not simple for iron, there is a significant effect of magnetism which must be taken into account.

Self–diffusion in austenitic iron follows the Arrhenius law (Fig. 11) over the temperature range 910–1400 °C for which experimental data exist. A comprehensive analysis of the experimental data by Oikawa [13,14] gave the following estimates for the diffusion parameters:

$$D = (0.89^{+0.40}_{-0.28}) \times 10^{-4} \exp\{-Q/RT\} \qquad \mathrm{m^2\,s^{-1}} \qquad \text{with} \qquad Q = 291.3 \pm 4.5\,\mathrm{kJ\,mole^{-1}} \quad (7)$$

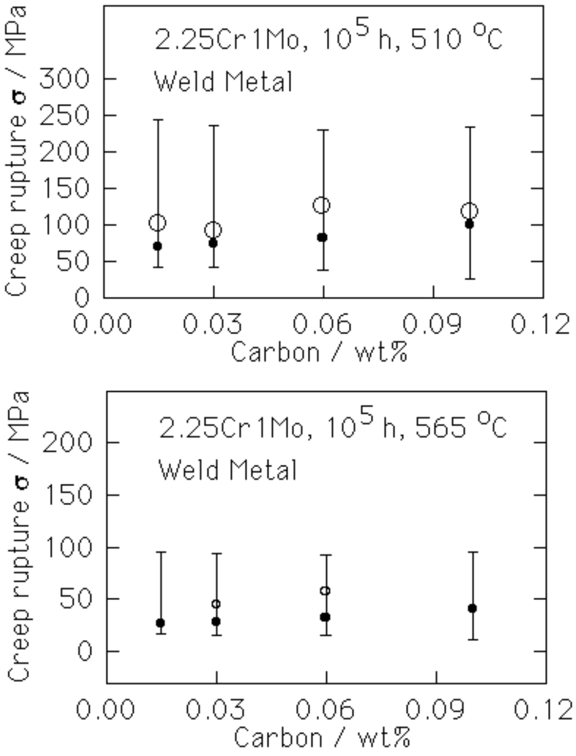

Fig. 9: Calculated (filled circles with error bars) and measured (open circles) stress rupture data for 2.25Cr1Mo weld metal.

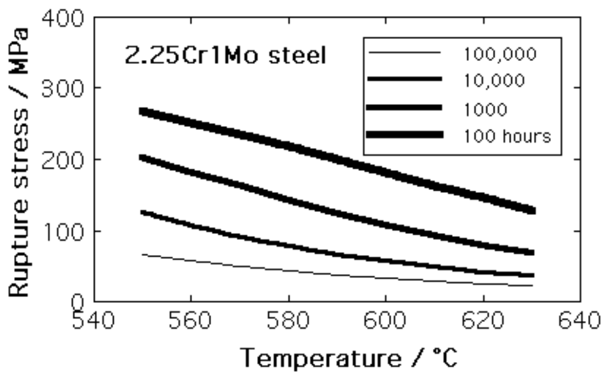

Fig. 10: Calculated stress rupture data for 2.25Cr1Mo weld metal.

The activation energy† for diffusion is larger than that of ferrite even though the melting temperature of austenite is slightly lower than that of ferrite. This is presumably because austenite is more densely packed than ferrite.

By contrast, the self–diffusion data for ferrite show considerable anomalies, both in the region

† Strictly an enthalpy, since the entropy terms are usually incorporated in the pre–exponential term. The activation enthalpy Q will therefore be distinguished from the activation free energy G^*.

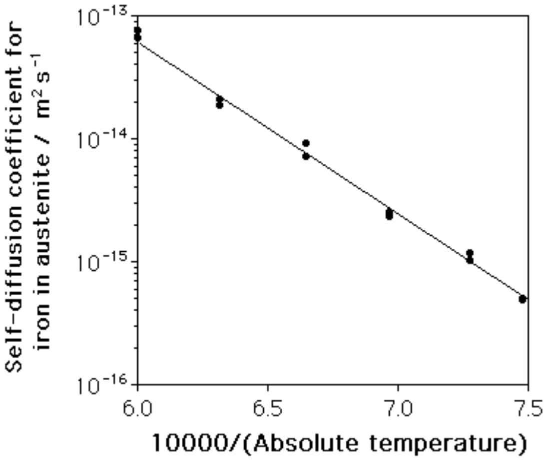

Fig. 11: Self–diffusion in austenite (data from [15]).

of paramagnetic to ferromagnetic transition and in the $\delta-$ferrite temperature range Fig. 12 [15,16,17]. The anomaly has been observed also for the diffusion of nickel in ferrite [18] and in a vast range of other measurements including mechanical properties such as creep at elevated temperatures.

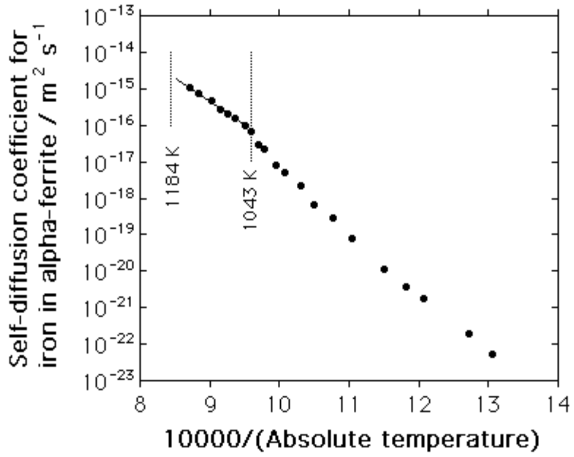

Fig. 12: Self–diffusion coefficient of iron in $\alpha-$ ferrite [17]. The Curie temperature is 1043 K and the formation of austenite begins at 1184 K.

Borg and Birchenall [16] suggested that both the vacancy formation energy and its ability to migrate are reduced in the ferromagnetic state. A theory which accounts for the effects in terms of pairwise magnetic interactions was proposed by Girifalco [19] and later by Ruch *et al.* [20]. For the fully ordered ferromagnetic state, the magnetic interaction energy of an atom which has N_c nearest neighbours is

$$W = -N_c s_0 \tag{8}$$

where $-s_0$ is the interaction energy per pair of atoms. This equation is based on the reasonable assumption that only near neighbour terms contribute significantly to W. When a vacancy is created by removing an atom, N_c pairs of contacts are broken, half of which are recreated when the discarded atom is replaced at the free surface. The enthalpy of formation of a vacancy is therefore increased by $\frac{1}{2}N_c s_0$. A similar argument gives a further contribution to the migration energy as $(N_v - N_*)s_0$ where N_v is the number of nearest neighbours to an atom paired with a vacancy, and N_* the number of nearest neighbours to an atom in its activated state, neglecting relaxation effects. The value of s_0 is proportional to the square of the saturation magnetisation $M_m\{0\}$ at absolute zero. Bearing this is mind, the activation enthalpy for self diffusion becomes

$$Q = Q_0 \left[1 + b_1 \left(\frac{M_m\{T\}}{M_m\{0\}} \right)^2 \right] \tag{9}$$

where Q_0 is the activation energy when there is no long range magnetic order (*i.e.* for paramagnetic ferrite). The constant b_1 is obtained by fitting to experimental data; it can in principle be partitioned into two components, one representing the increment (due to magnetic spin order) in the vacancy formation energy and the other in the migration energy. This is difficult to do in practice because the calculations require a knowledge of the saddle point configuration during the migration over the activation barrier. The important point is that equation 9 gives a temperature dependence to the activation energy, making it possible to interpret the deviations from the Arrhenius relationship.

Very precise measurements by Iijima *et al.* [17] confirm the relation over a wide temperature range (766–1148 K), with $Q_0 = 250.6 \pm 3.8\,\mathrm{kJ\,mol^{-1}}$, $b_1 = 0.156 \pm 0.003$ and the pre–exponential factor in the Arrhenius equation given by $D_0 = (2.76\,^{+1.42}_{-1.04}) \times 10^{-4}\,\mathrm{m^2\,s^{-1}}$ (Fig. 12). The temperature dependence of the self–diffusion coefficient apparently shows the normal Arrhenius relationship above the Curie temperature. Magnetisation data are necessary to use this diffusion model; these have been reported, for example, by Potter [21] and Crangle and Goodman [22].

There are two further issues which need to be considered. Firstly, early research had indicated that the diffusion anomaly extends to temperatures beyond the Curie temperature, which would be inconsistent with a theory which relies on just the the long–range magnetic–order parameter since the magnetisation terms then tends to zero towards T_c. Modern high–precision measurements on well prepared samples do not reveal anomalous effects beyond T_c.

Secondly, measurements for δ–ferrite at very high temperatures do not fit the extrapolated data for paramagnetic α–ferrite (Fig. 13). Instead, for δ–ferrite it is found that $D_0 = 9.21 \times 10^{-3}\,\mathrm{m^2\,s^{-1}}$ with a higher activation energy of $Q = 296\,\mathrm{kJ\,mol^{-1}}$. It has been postulated that at high temperatures diffusion by a divacancy mechanism makes a contribution which is additional to that from the usual monovacancy mechanism [17], though an alternative explanation is that the neglect of short–range order effects near T_c gives an error in the slope of the Arrhenius plot for much higher temperatures. Nevertheless, the precision of the measurements made by Iijima and co–workers casts some doubt on whether a diffusion anomaly exists for $T > T_c$. Similar observations have been reported for the self–diffusion in cubic close–packed cobalt, where the diffusion anomaly is very small indeed when compared with iron. In spite of this, the Arrhenius plot curves upwards as the melting temperature is approached, supporting the hypothesis of an increasing contribution from the divacancy mechanism [23]. The estimated values of the diffusion parameters for self–diffusion by the divacancy mechanism in ferrite are:

$$D_{2v} = 5.2 \exp\left\{ -\frac{406,000}{RT} \right\} \qquad \mathrm{m^2\,s^{-1}} \tag{10}$$

where the units of the activation energy are in $\mathrm{J\,mol^{-1}}$. This makes D_{2v} about half D_v at the melting temperature.

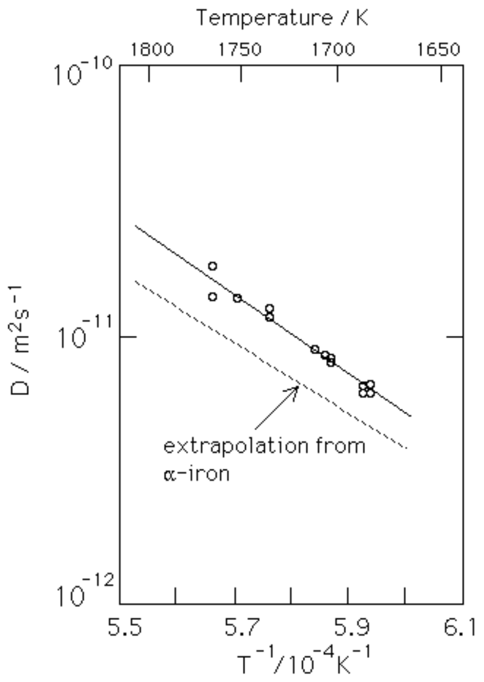

Fig. 13: Self–diffusion coefficient of iron in $\delta-$ ferrite [17]. The $\gamma \rightarrow \delta$ transformation occurs at 1665 K and melting at 1811 K.

Short–range magnetic order persists to temperatures well in excess of the Curie temperature. A number of models have been proposed which account for short–range order effects and at the same time allow δ–ferrite and paramagnetic α–ferrite to be treated identically. The models do involve a larger number of fitting parameters. In addition they do not seem to explain why the diffusion anomaly vanishes at $T/T_c \simeq 1.16$, whereas the short range order parameter remains significant to even higher temperatures (Fig. 14).

To cope with this latter difficulty, Kučera [24] defined a fictitious paramagnetic temperature ($T_p > T_c$) beyond which there is no measurable effect on diffusion of (short–range) magnetisation with

$$Q = Q_0(1 + q\{T\}) \tag{11}$$

with the complicated function $q\{T\}$ being such that contributions from long–range order go to zero at T_c and those from short–range order become zero at T_p. Zener [25] argued for a temperature dependent activation free energy because an atom during its course of migration strains the surrounding lattice, and the resistance of the lattice to such deformation changes with temperature. He further suggested that the temperature coefficient of the ratio G^*/G_0^* should therefore be the same as that of the shear moduli μ_e/μ_e^o, where in each case the subscripts indicate the value at $T = 0$. Any temperature dependence of the activation free energy can be incorporated into the pre–exponential term in the diffusion coefficient via the activation entropy, the change in which becomes:

$$\Delta S^* \simeq \frac{b_2}{T_m}\frac{d(\mu_e/\mu_e^o)}{d(T/T_m)} \tag{12}$$

where T_m is the melting temperature and b_2 is a fitted constant. Since the shear modulus also depends on the magnetic state, Kučera incorporated the function $q\{T\}$ in the pre–exponential factor as well:

$$D = D_0 \exp\left\{\frac{0.35q\{T\}Q_0}{RT_m}\right\}\exp\left\{-\frac{Q}{RT}\right\} \tag{13}$$

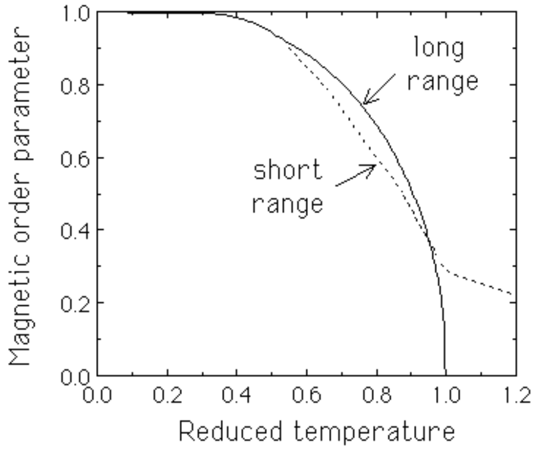

Fig. 14: The calculated long–range and short–range magnetic order parameters for bcc iron [24]. The reduced temperature is the ratio of the absolute temperature to the Curie temperature.

Other models have involved empirical modifications of the Kučera approach, for example by substitution of the excess enthalpy attributed to the magnetic effect for the function $q\{T\}$ whilst retaining the same form as equation 13 [26], or by explicitly including the shear moduli in the calculations [27,28]. Some models include two additional terms in the activation energy function, one containing the variation in the long range order parameter and the other the variation in the elastic modulus ([28,29]. Jönsson [30] pointed out that these models are difficult to distinguish as empirical representations because the excess enthalpy and elastic modulus vary in a similar manner with the temperature. Neither the excess enthalpy nor the difference in shear moduli between the ferromagnetic and paramagnetic states reach zero at the temperature where the diffusion anomalies vanish.

Bearing in mind that enthalpy data are more frequent than modulus data for alloys, Jönsson adapted Braun and Feller–Kniepmeier's method where the diffusion anomaly is expressed purely as a function of the excess enthalpy, so that in equation 13 the function q becomes

$$q\{T\} = b_3 \ {}^{mg}\Delta H\{T\}$$

where b_3 is a fitting constant and ${}^{mg}\Delta H\{T\}$ is the excess magnetic enthalpy at the temperature T. Equation 13 contains the melting temperature whose meaning in the context of diffusion is not clear for an alloy where melting occurs over a range of temperatures. However, there is a well known empirical relationship between the activation energy for diffusion and the melting temperature of a pure metal,

$$Q_0 = 140T_m \qquad \mathrm{J\,mol^{-1}}$$

so that the melting temperature can be eliminated from equation 13. By fitting the equation to ferritic iron, Jönsson was able to demonstrate that with appropriate thermodynamic data for ${}^{mg}\Delta H$†, he was able to estimate fairly well the tracer diffusion of elements such as cobalt, nickel in ferrite both in the ferromagnetic and paramagnetic regions. The activation energy and D_o for the paramagnetic state derived by fitting in each case but b_3 was kept fixed, assumed to depend only on the lattice geometry.

To summarise, it is possible, when the thermodynamic data necessary for the estimation of ${}^{mg}\Delta H\{T\}$ are available, to calculate the effect of solute elements on the tracer diffusion coefficient of iron. It will be interesting to see how such information can be exploited in the design of creep–resistant steels.

Acknowledgments

I am grateful to the organisers Andrew Strang and Malcolm Mclean for the excellent organisation and for financial support. It is a pleasure also to acknowledge very useful discussions with Dr Joe Robson and Mr Dave Cole.

Conclusions

It is now possible to attempt a quantitative design of heat resistant steels and welding alloys. This is true both with respect to the kinetics of microstructural evolution and in the estimation of creep rupture strength. The combined models provide for the first time an ability to predict new alloys. It would now be interesting for industry to set some challenges, which would stimulate theoretical predictions and finally experimental verification. The whole process from the conception of an alloy to its verification should take much less time than has previously been the case.

In the longer term it is necessary for the microstructure models to predict particle size and spatial distributions, and the effect of stress and strain on transformation kinetics. Such information can then be used in a more sophisticated mechanical model, perhaps based on dislocation and recovery theory.

References

1. MTDATA: *Metallurgical Thermochemistry Group,* National Physical Laboratory, Teddington, London (1998)
2. S. D. Mann, D. G. McCulloch and B. C. Muddle: *Metallurgical and Materials Transactions A* 26A, 509–520(1995)
3. A. Strang and V. Vodarek: *Materials Science and Technology,* 12, 552–556.(1996)
4. J. D. Robson and H. K. D. H. Bhadeshia: *Mat. Sci. Tech.* 13, 631–644(1997)
5. J. W. Christian: *Theory of Transformations in Metals and Alloys,* Pergamon Press, Oxford, 2nd edition, part I (1975)
6. H. K. D. H. Bhadeshia: *Materials Science and Technology* 5, 131–137.(1989)
7. N. Fujita and H. K. D. H. Bhadeshia: *Advanced Heat Resistant Steels for Power Generation,* San Sebastian, published by the Institute of Materials, London, in press.(1998)
8. R. G. Baker and J. Nutting: *Journal of the Iron and Steel Institute* 192, 257–268(1959)
9. F. Brun, T. Yoshida, J. D. Robson, V. Narayan and H. K. D. H. Bhadeshia: *Materials Science and Technology* submitted(1998)
10. D. Cole and H. K. D. H. Bhadeshia: *Unpublished research,* University of Cambridge (1998)

† a function of the Curie temperature and the magnetic moment per atom.

11. D. J. C. MacKay: *Neural Computation* 4, 415-472(1992)
12. C. D. Lundin, S. C. Kelley, R. Menon and B. J. Kruse: *Welding Research Council bulletin 277,* New York 1–66(1986)
13. H. Oikawa: *Technical Report, Tohoku University, Japan,* 47, 67–77, 215–224.(1982)
14. H. Oikawa: *Technical Report, Tohoku University, Japan,* 48, 7–77.(1983)
15. F. S. Buffington, K. Hirano and M. Cohen: *Acta Metallurgica,* 9 434–439.(1961)
16. R. J. Borg and C. E. Birchenall: *Trans. TMS–AIME* 218, 980–984.(1960)
17. Y. Iijima, K. Kimura and K. Hirano: *Acta Metallurgica,* 36, 2811–2820.(1988)
18. K. Hirano, M. Cohen and B. L. Averbach: *Acta Metallurgica,* 9 440–445.(1961)
19. L. A. Girifalco: *Journal Phys. Chem. Solids* 23, 1171–1173.(1962)
20. L. Ruch, D. R. Sain, H. L. Yeh and L. A. Girifalco: *J. Phys. Chem. Solids,* 37, 649–653.(1976)
21. H. H. Potter: *Proc. Roy. Soc. Lond.,* 146, 362–387.(1934)
22. J. Crangle and G. M. Goodman: *Proc. Roy. Soc. Lond.,* A321, 477–491.(1971)
23. C.-G. Lee, Y. Iijima and K. Hirano: *Defect and Diffusion Forum,* 95–98, 723–728.(1993)
24. J. Kučera: *Czech. J. Physics,* B29, 797–809.(1979)
25. C. Zener: *Imperfections in nearly perfect crystals,* eds W. Shockley, J. H. Holloman, R. Maurer and F. Seitz, John Wiley and Sons Inc., New York, 289–314.(1952)
26. R. Braun and M. Feller–Kniepmeier: *Scripta Metall.,* 20, 7–12.(1986)
27. H. V. M. Mirani, R. Harthhoorn, T. J. Zuurendonk, S. J. Helmerhorst and G. de Vries, : *1975* 29,(Phys. Stal. Sol. (a),) 1975 115–120.
28. J. Cermak, M. Lubbenhusen and H. Mehrer: *Z. Metallkunde,* 80, 213–219.(1989)
29. M. Lübbehusen and H. Mehrer: *1990* 38,(Acta Metall. Mater.,) 1990 283–292.
30. B. Jönsson: *Z. Metallkunde,* 83, 349–355.(1992)